Journal of Nuclear Materials 490 (2017) 260–271

Contents lists available at ScienceDirect

Journal of Nuclear Materials

journal homepage: www.elsevier.com/locate/jnucmat

Irradiation effects in beryllium exposed to high energy protons of the NuMI neutrino source

V. Kuksenko [a, *], K. Ammigan [b], B. Hartsell [b], C. Densham [c], P. Hurh [b], S. Roberts [a]

[a] University of Oxford, Oxford, UK
[b] Fermi National Accelerator Laboratory, Batavia, USA
[c] Rutherford Appleton Laboratory, Didcot, UK

ARTICLE INFO

Article history:
Received 16 December 2016
Received in revised form
30 March 2017
Accepted 10 April 2017
Available online 13 April 2017

Keywords:
Beryllium
Proton irradiation
Neutrino targets
EBSD
EDS
Atom probe tomography
Transmutation elements
Precipitation
Segregation

ABSTRACT

A beryllium primary vacuum-to-air beam 'window' of the "Neutrinos at the Main Injector" (NuMI) beamline at Fermi National Accelerator Laboratory (Fermilab), Batavia, Illinois, USA, has been irradiated by 120 GeV protons over 7 years, with a maximum integrated fluence at the window centre of 2.06 10^{22} p/cm^2 corresponding to a radiation damage level of 0.48 dpa. The proton beam is pulsed at 0.5 Hz leading to an instantaneous temperature rise of 40 °C per pulse. The window is cooled by natural convection and is estimated to operate at an average of around 50 °C. The microstructure of this irradiated material was investigated by SEM/EBSD and Atom Probe Tomography, and compared to that of unirradiated regions of the beam window and that of stock material of the same PF-60 grade.

Microstructural investigations revealed a highly inhomogeneous distribution of impurity elements in both unirradiated and irradiated conditions. Impurities were mainly localised in precipitates, and as segregations at grain boundary and dislocation lines. Low levels of Fe, Cu, Ni, C and O were also found to be homogeneously distributed in the beryllium matrix. In the irradiated materials, up to 440 appm of Li, derived from transmutation of beryllium was homogeneously distributed in solution in the beryllium matrix.

1. Introduction

It is now recognized that materials degradation by radiation damage is one of the most challenging factors in the design and operation of next generation multi-megawatt high intensity proton accelerator facilities [1]. The existing database on materials response to radiation effects relevant to proton accelerator environments is very limited and this complicates material selection and lifetime predictions for beam windows and targets. An international research collaboration, Radiation Damage In Accelerator Target Environments (RaDIATE), was recently launched in order to explore radiation damage issues in different candidate materials under the relevant environment [2]. Beryllium is an excellent beam window material due to its high strength, low atomic number, low nuclear interaction cross-section and high melting point, and this paper reports the study of one such successful application. Beryllium is an alternative to graphite in applications where a low-Z particle production target material is appropriate (e.g. the NuMI pion production target). Consequently Be has been selected as one of very few candidates for beam windows and target components in a new generation of proton accelerator driven particle sources such as, for example, the Long Baseline Neutrino Facility (LBNF) [1,3,4], a higher power version of NuMI.

Industrial purity beryllium grades used in accelerator components contain a wide variety of trace impurities, typically oxygen, iron, aluminium, nickel, copper, silicon, carbon and magnesium. The majority of these impurities have very limited solubility in beryllium, and have strong tendencies to create precipitates and to segregate to defects such a grain boundaries or dislocations [5]. This may have significant deleterious effects on mechanical properties. For example:

1. Hard BeO particles play a role of stress concentrator sites and fracture origins, and the quantity, size and distribution of BeO particles can strongly affect the mechanical properties of beryllium [5]. Webster [6] also demonstrated that dispersed BeO

* Corresponding author.
E-mail address: viacheslav.kuksenko@materials.ox.ac.uk (V. Kuksenko).

http://dx.doi.org/10.1016/j.jnucmat.2017.04.011
0022-3115/

particles control grain boundary migration and, consequently, grain size stability of beryllium.
2. Phases containing Fe and Al also have significant influence on mechanical properties of beryllium. X-ray diffraction studies of Jones and Weiner [7] of commercial beryllium after different heat treatments showed a link between the strain induced precipitation of the Be_5(FeAl) phase and the decrease in tensile ductility and creep strength of the samples. Punni and Cox [8] studied corrosion properties of several beryllium grades and demonstrated that the Fe/Al/Be inclusions were the preferential sites for pit corrosion initiations.
3. Fe-Be-rich precipitates can lock dislocations and increase hardness of beryllium alloyed by iron, as was demonstrated by Morozumi and co-workers [9].

It is well-known that radiation damage, introduced by high-energy particles can change the quantity, size, spatial distribution and chemistry of phases present in the microstructure and, thus, the properties of exposed materials [10]. Although it is established that radiation generally leads to evolution of the properties of beryllium [11–13], the mechanisms underlying these changes are not well understood; for example, data about the stability of precipitates under radiation is very limited. No experimental data are currently available on phase stability under irradiation conditions relevant to beryllium components of particle accelerators (e.g. windows, targets).

Interactions of high-energy neutrons or protons with matter induce transmutation reactions. In the case of beryllium, most attention is currently paid to the gas transmutation products hydrogen and helium. Helium accumulation from either direct ion implantation or as a result of neutron-induced transmutation has been shown to result in significant changes in the properties of beryllium over a wide range of temperatures [14–17]. Such effects include those from the formation of nanosized helium bubbles, which is believed to be one of the main hardening mechanisms of beryllium irradiated at low temperatures [17]; additionally, helium assisted anisotropic swelling at low temperatures and helium bubble formation at grain boundaries at high temperatures may lead to grain boundary weakening and drastic loss of ductility [15,18]. The production rate of helium in beryllium under fission and fusion neutron irradiation conditions can be as high as 600 appm/dpa (displacements per atom) [19]. However, as presented here in section 3, in a high energy proton irradiation environment it can reach 4000 appm/dpa with thus a potential for even greater degradation of mechanical properties.

Non-gaseous transmutants can also alter the microstructure of irradiated materials and potentially lead to property degradation. This has been studied in a wide range of metallic alloy systems. For example, Ohnuki and co-workers observed that formation of Cr by transmutation reaction in V-alloys during irradiation in the High Flux Isotope Reactor (HFIR) caused very high embrittlement of the exposed alloys [20–22]. Works of Garner, Greenwood and Edwards have demonstrated that Mo-Re alloys strongly transmute to Mo-Re-Os-Ru-Tc system in a fast neutron spectra of the Fast Flux Test Facility (FFTF) that had serious consequences on the alloys phase stability. The transmutant osmium shows a strong tendency to co-segregate with Re under irradiation [23,24] potentially contributing to radiation induced embrittlement of the Mo-Re alloys [25]. Studies of ferritic-martensitic (FM) steel after mixed spectrum irradiation of high energy protons and spallation neutrons of the Swiss spallation neutron source (SINQ) showed that transmutants Ca, Sc and Ti extensively participate in the evolution of the microstructure through formation of radiation-induced clusters, segregation at the dislocation loops and alteration of the micro-chemistry of carbides [26], resulting in hardening and loss of ductility of the irradiated materials [27]; however, it was not possible to separate the influence of displacement damage, helium production and solid transmutant effects. To our knowledge, there are no data regarding the behaviour of solid transmutation products formed in beryllium. This work reports on the microstructure of industrial purity beryllium and changes induced by high-energy proton irradiation in the "Neutrinos at the Main Injector" (NuMI) beamline [28] at Fermilab, Batavia, Illinois.

2. Materials and techniques

2.1. Materials

The material used in this work is the industrial PF-60 beryllium grade. Its nominal chemical composition as specified by the manufacturer (Materion Electrofusion Corporation) is specified in Table 1 [29]; the main specified impurities are O (up to 2900appm), C (up to 450appm), N (up to 195 appm), Al (up to 165 appm), Fe (up to 130 appm) Si (up to 130 appm) and Mg (up to 81 appm).

A disk of PF-60 of 0.25 mm thickness served as a primary beam window in the NuMI beam line for 7 years from May 2005 till April 2012. It was exposed to a 120 GeV pulsed proton beam. The pulse frequency was 0.5 Hz, with a total pulse length of 9.78 μsec or 8.14 μsec for different operational modes, and with each pulse consisting of 6 or 5 batches respectively. Each batch was separated in time from the other by about 56 nsec, and consisted of 84 bunches with a spacing of 18.8 nsec. Each pulse delivers about 3×10^{13} protons. The final integrated exposure of the window reached 1.57×10^{21} protons. The beam had a Gaussian profile with the approximate size (as standard deviation of the distribution from the centre) $\sigma_x = \sigma_y = 1.1$ mm. Over the 7 years of operation, the position of the beam was changed several times for better adjustment to the position of targets and horns. These shifts were less than half of the beam sigma away from the central position for about 95% of total beam exposure. Although, the working temperature cycled with the pulsing of the proton beam, the average working temperature of the window was estimated to be approximately 50 °C over the last half of its operating period.

The displacement damage levels and concentrations of transmutation products were assessed using the Monte-Carlo MARS15 code [30–32]. The code calculates the number of displacements based on the NRT model [33] using an energy-dependent damage efficiency function (see Ref. [34] for details). The predicted maximum radiation damage level in the central part of the window was about 0.48 dpa, which, considering the beam position changes, decreases to the periphery following an almost Gaussian profile with $\sigma \approx 1.2$mm, giving a wide spectrum of radiation doses at almost the same temperature. The exposed area was experimentally localised using Gafchromic dosimetry film (type HD-V2) as shown in Fig. 1(b).

After irradiation, the central part of the beam window was punched out from its mounting flange. The applied stresses during this procedure caused deformation of the central part of the window and development of radial cracks as shown on Fig. 1(a). The sample remained in one piece overall, with no obvious fragmentation. The cracks were used for investigation of fracture behaviour of beryllium in the unirradiated areas and those exposed to varying levels of radiation damage.

For the investigation of non-irradiated beryllium, two complementary studies were made:

1. Material from outer areas of the NuMI window, at least 8 mm from the centre of the exposed area i.e. not exposed to proton irradiation, was investigated by atom probe mapping, S (TEM)/EDS and study of the fracture paths;

Table 1
Nominal and APT-measured chemical compositions of PF-60 beryllium in the un-irradiated state and after irradiation to different doses.

Impurity Element	Concentration			
	Nominal maximum content, appm [29]	APT measurements, appm		
		0 dpa	0.41 dpa	0.46 dpa
C	450	15 ± 10	cannot be measured	cannot be measured
Cu	14	14 ± 10	17 ± 10	21 ± 10
Fe	130	55 ± 10	47 ± 10	55 ± 10
Ni	31	23 ± 10	20 ± 10	45 ± 20
O	2900	70 ± 30[a]	67 ± 30	90 ± 30
Li	4	ND[b]	400 ± 20	440 ± 20
Others	Ag = 1, Al = 165, B = 2.5, Ca = 22, Cd = 05, Co = 1.5, Cr = 17, Si = 130, Mg = 81, Mn = 17, Mo = 2, N = 195, Pb = 1	ND	ND	ND
Non-identified new isotopes in the irradiated state[c]: Peaks at (Da): 13, 14, 15, 15.5, 16.5 19, 19.5, 20, 20.5, 21, 21.5, 22, 22.5, 23, 23.5, 24, 26, 31, 32, 33, 34	–	–	170 ± 40	190 ± 40
Be	balance	balance	balance	balance

[a] the value may include oxygen contamination from the experimental analysis chamber.
[b] Not detected.
[c] isotopes of hydrogen and molecular ions of hydrides of beryllium have not been quantified.

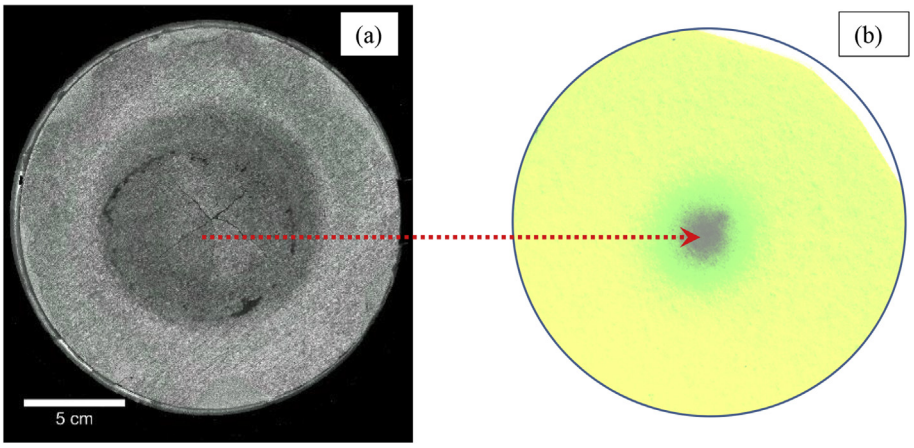

Fig. 1. (a) NuMI beam window and (b) a dosimetry film exposed for approximately 150 h by activated areas in the window. Cracks, developed during the post-irradiation specimen extraction procedure, are visible in image (a). The central part of the irradiated area in image (b) is predicted to correspond to about 0.48dpa of radiation damage.

2. The same PF-60 beryllium grade produced by the same manufacturer, but from a different batch, was studied by (S) TEM/EDS and SEM/EBSD/EDS for detailed investigation of its grain structure and for microscopic chemical mapping.

2.2. Techniques

Grain size, texture, distribution of chemical elements and crack paths were examined using a TESCAN MIRA3 SEM equipped with Oxford Instruments Energy Dispersive X-ray Spectroscopy (EDS) and Electron Backscatter Diffraction (EBSD) detectors in the National Nuclear User Facility (NNUF) Materials Research Facility (MRF) at the Culham Centre for Fusion Energy (CCFE) and a JEOL 840 A scanning electron microscope equipped with EDAX-TSL EBSD system and INCA EDS systems at Oxford University Materials Department. Because of the very poor sensitivity of EDS systems to beryllium and other light elements, only a qualitative analysis of EDS results has been made. Fine-scale chemical mapping was done on the JEOL JEM-2100 transition electron microscope equipped with an Oxford instrument EDS detector.

Suitable surface conditions for SEM/EDS and SEM/EBSD analysis of as-received non-irradiated PF-60 samples were obtained by sequentially mechanically grinding and polishing with SiC paper, diamond paste and colloidal silica. Unirradiated and irradiated areas of the proton irradiated NuMI window sample were prepared by Focused Ion Beam (FIB) removal of surface oxide and contamination, and subsequent FIB polishing. During the FIB surface preparation, the sample was tilted to about 25° from the Ga ion beam. It was established that final polishing with a 30 keV, 9 nA beam produces a surface quality suitable for chemical and crystallographic analysis of grains. OIM TSL software was used for analysis of the EBSD data. A grain dilation algorithm was used for data clean-up; this method allows modification of orientations of incorrectly indexed points, particularly at grain boundaries.

Samples for atom probe tomography (APT) examination [35,36] were prepared in the CCFE MRF using a FEI Helios FIB system dedicated for use with radioactive and toxic materials. Initially a 25 μm × 7 μm foil, 2 μm in thickness was lifted out from the irradiated sample. 2 μm × 2 μm × 7 μm columns were then cut from the foil and individually welded by Pt deposition to silicon posts. Annular milling was used to obtain sharp tips suitable for APT analysis.

The 3D distribution of chemical constituents was studied using a

LEAP 3000 APT system. The analyses were performed using laser pulses with a 0.55 nJ energy and a pulse repetition rate of 200 kHz on specimens cooled to 30–50 K. The pulse energy was chosen after preliminary experiments established that it gave the highest full-width at half maximum mass resolution for the main beryllium peak ($9Be^{++}$) and lowest level of background noise. The total analysed volume corresponded to about 100 million collected ions each for the as-received and the irradiated beryllium.

Analysis of the APT data was performed using IVAS 3.6.8 software. Specimen regions unaligned with major crystallographic poles were used for the statistical analyses. The homogeneity or otherwise of elemental distributions was firstly estimated by visual inspection of spatial distribution maps and then analysed in detail by χ^2 analysis [37], using box sizes of 100 ions, and First Nearest Neighbour distribution analysis [36].

3. Experimental results

3.1. Unirradiated material

Fig. 2 shows images of the grain structure in as-manufactured PF-60 beryllium, using optical microscopy (polarised light) and SEM/EBSD. Grains have irregular but roughly equiaxed shapes with a broad size distribution; some twins are present. Grain boundaries with misorientation more than 15° are highlighted by black lines in Fig. 2(b). The mean grain diameter in this plane is 25 ± 14 μm. The EBSD inverse pole image in Fig. 2(b) shows that this beryllium grade has crystallographic texture with a preferential orientation of the basal plane (0001) close to the plane of observation. This texture results from the hot rolling used for forming the PF-60 sheet [29]. EBSD contrast changes inside grains originate from internal strains and low-angle grain boundaries indicating that the material is not fully recrystallized after hot rolling.

Fig. 3 shows SEM and EDS scans of a typical area. SEM confirms the broad distribution of the grains size revealed by the EBSD analysis and the presence of twins (thin elongated grains on Fig. 3(a)). Precipitates are mainly located inside grains rather than at grain boundaries. They are mainly localised in small, often elongated agglomerates, and have white contrast in secondary electron imaging. EDS mapping shows that the majority of these precipitates are enriched with oxygen, aluminium, iron, silicon and titanium that, as will be discussed later, is in good agreement with very limited solubility of these impurities in beryllium [5]. The mixture of these elements is highly variable between precipitates. EDS maps of nickel and copper showed that these elements are homogenously distributed in the beryllium matrix. Although the room temperature solubility of these elements has never been measured, extrapolation of high-temperature data suggests their moderate solubility in beryllium (up to few atomic percent [5]) that correlates with the EDS maps.

Since precise quantification of beryllium and other low-Z elements is not possible with EDX systems, only a qualitative characterisation of the precipitates can be made. Oxygen-enriched particles were usually localised in agglomerations in grain interiors (Fig. 3(b)), and are likely to be beryllium oxide (BeO). SEM/EDX chemical maps also show that the oxygen-containing precipitates are often enriched by aluminium, silicon and iron.

Fig. 4 shows high resolution STEM/EDS maps, revealing that at least in the larger oxide particles (over a few hundred nanometres diameter), Al and Si are not homogeneously distributed inside the oxides, but rather are present as an Al-Si enriched shell, with a thickness of several tens of nanometres, around oxygen enriched cores. In addition, high resolution STEM/EDS investigation revealed that beryllium oxide particles are also carbon-enriched.

Figs. 3(d,e) and 4(d,e) also show a separate family of Al-Fe precipitates. Quantitative analysis of EDS data shows that the Al:Fe ratio in these objects is in the range 1.2–1.45. These precipitates may be also enriched by Si, O, C, Ti and Cr. A third type of precipitate is rich in Si (Fig. 4(e)); all the precipitates of this type were found in close proximity to BeO particles, so it was not possible to determine whether they are elemental silicon, as found by Rooksby and Green [38], or silicon oxide.

As well as forming precipitates, Fe also segregates to grain boundaries. Fig. 4(g) shows an Fe count rate profile across a grain boundary; the intensity of Fe counts at the grain boundary is remarkably higher than inside the grains. However, these data cannot be used to quantify values for Fe grain-boundary segregation, because: (i) EDS systems cannot reliably quantify beryllium (the main material constituent); (ii) the Fe signal is averaged over the overall depth of the sample. Systematic site-specific atom probe tomography would be needed to give a quantitative characterisation of grain-boundary segregation behaviour.

Atom probe tomography was also used to quantify impurity concentrations inside the beryllium grains. Mass-spectrum peaks of carbon, oxygen, iron, nickel and copper were identified, and the concentrations of these impurities are shown in Table 1. The concentrations of Ni and Cu are in good agreement with the nominal composition data, which also correspond to those observed as homogeneous distributions by EDS. For other elements, the matrix compositions measured by APT (Fe: 55 appm; O: 70 appm) are significantly lower than the nominal chemical compositions, correlating with their very limited solubility and tendency to form

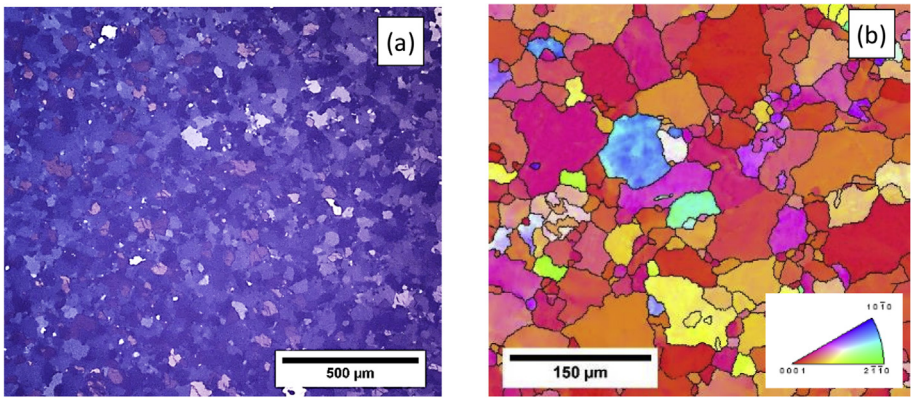

Fig. 2. As-received PF-60 sheet: (a) Polarised-light optical microscopy image; (b) surface normal-projected inverse pole figure orientation map, with high angle grain boundaries (misorientation >15°) are highlighted by black lines; the material has a strong (0001) texture.

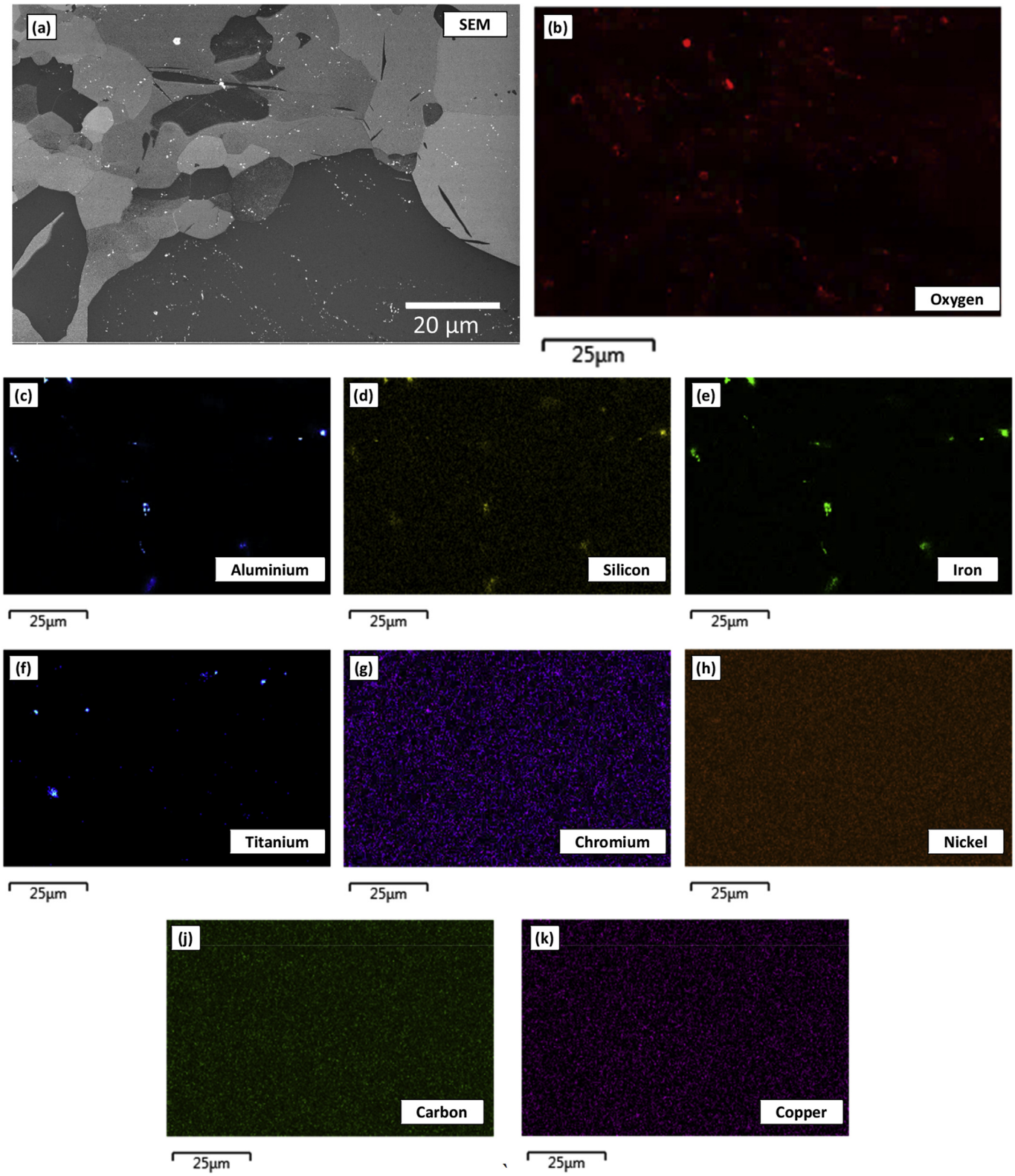

Fig. 3. (a) Secondary electron SEM image and (b–k) EDS chemical maps of a PF-60 beryllium sample in the as-received state. Precipitates have white contrast on the SEM image; the majority of the white contrast particles are enriched with oxygen, silicon, aluminium, and/or iron. Some precipitates enriched by titanium and, rarely, by chromium. (For interpretation of the references to colour in this figure legend, the reader is referred to the web version of this article.)

precipitates. It is possible that some fraction of the oxygen detected by APT could be due to contamination of the analysis chamber during the experiment.

Statistical analysis of 3D chemical maps demonstrated that these impurities are randomly distributed in the beryllium matrix. However, in one of analysed volumes (Fig. 5), a linear

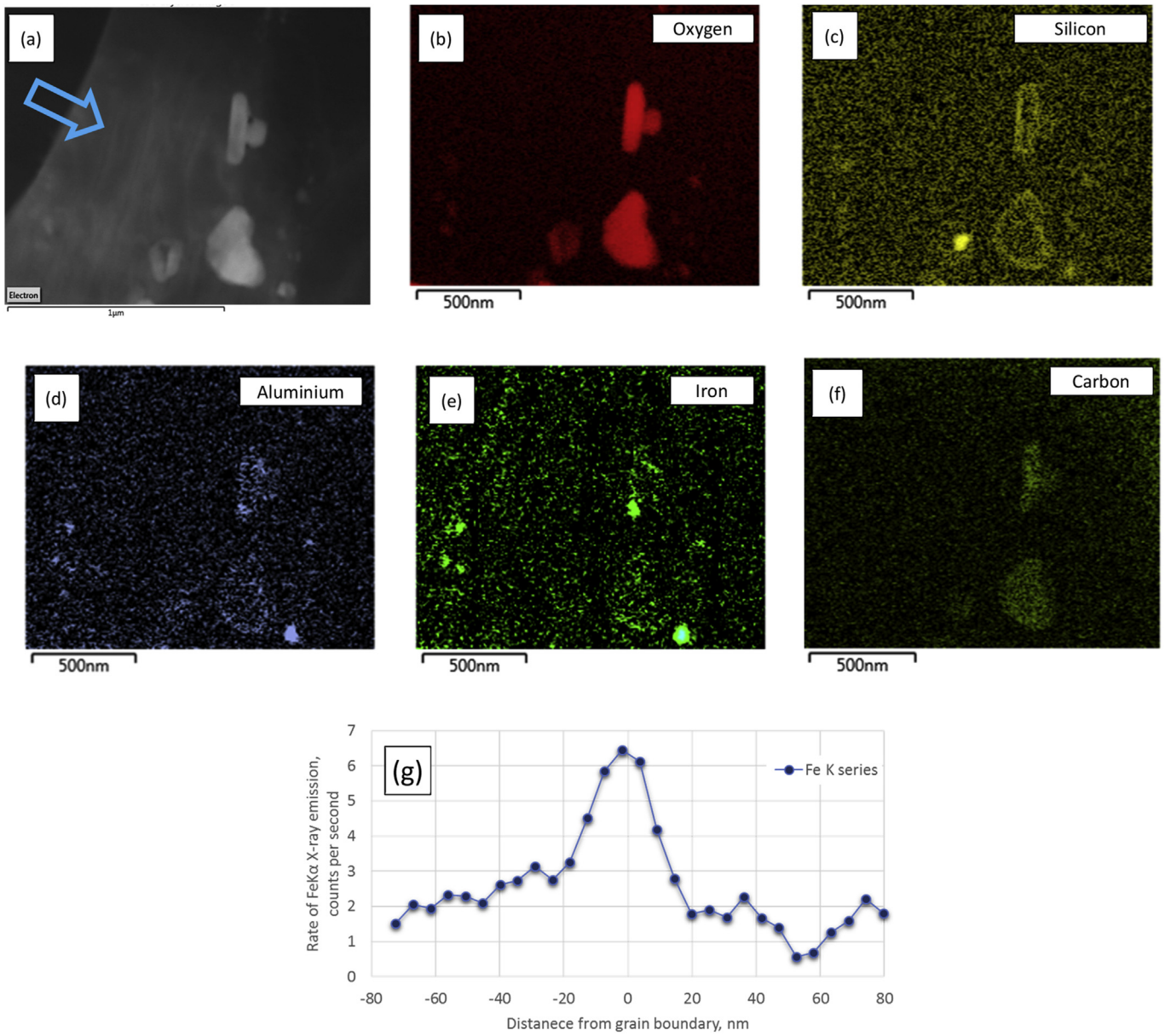

Fig. 4. (a) STEM image of a near-grain boundary area in unirradiated PF-60 beryllium from the periphery of the NuMI beam window. The grain boundary is largely free of precipitates; (b–f) EDS chemical maps show that the oxide particles are also enriched by Si, C, Fe and Al impurities and that larger particles have pronounced Al and Si segregation on surface. (g) a count rate profile for Fe taken across the grain boundary indicated by the blue arrow on (a).

agglomeration of iron atoms was detected, which is probably a segregation around a dislocation line. The radius of the detected segregation was about 1 nm, and the concentration of Fe within this region was at least 1 at% (10000 appm).

3.2. Proton irradiation effects in beryllium

Fig. 6 shows STEM/EDS analyses of PF-60 beryllium irradiated to 0.45 dpa. A wide variety of precipitates was detected, with compositions and distributions similar to those observed in the unirradiated material. The core-shell structure of the beryllium oxides was also present after irradiation. The only significant difference from the unirradiated material was that while all the detected grain boundaries in the non-irradiated state were enriched only by Fe, boundaries enriched also by aluminium were detected in the irradiated areas, (see Fig. 6 (d, e, f)). Since the mean grain size of the PF-60 grade (~25 μm) is significantly bigger than that of the FIB lamella for TEM investigation (~4 × 10 μm^2) and given the limited overall area that could be investigated by STEM, the apparent absence of Al segregation in the non-irradiated state may be due to statistical variations in sampling. Further investigations are ongoing.

The composition of the post-irradiation beryllium matrix was investigated via APT; data are given in Table 1. The main impurities present before irradiation (Fe, Ni, O, Cu) do not exhibit significant concentration changes after high-energy proton irradiation, and these elements were still homogeneously distributed in the matrix after irradiation.

Fig. 7 shows sections of two APT mass-spectra from the irradiated and non-irradiated areas of the NuMI beam window, where new peaks at 6 and 7 Da are visible only in the irradiated state. In the samples taken from the NuMI window areas irradiated to about 0.41 dpa, the mass-spectrum peaks at 6 Da and 7 Da represent

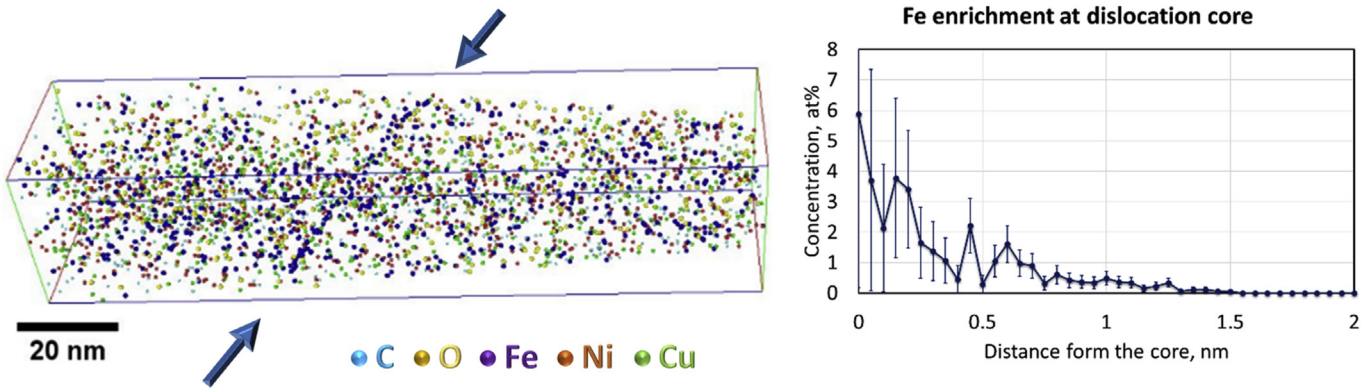

Fig. 5. (a) Atom Probe Tomography reconstruction of as-received PF-60 beryllium, showing only C, O, Fe, Ni and Cu atoms; the arrows indicate the position of a probable dislocation line; (b) iron radial concentration profile around the dislocation core. All the detected impurities, except Fe, are randomly distributed in the beryllium matrix.

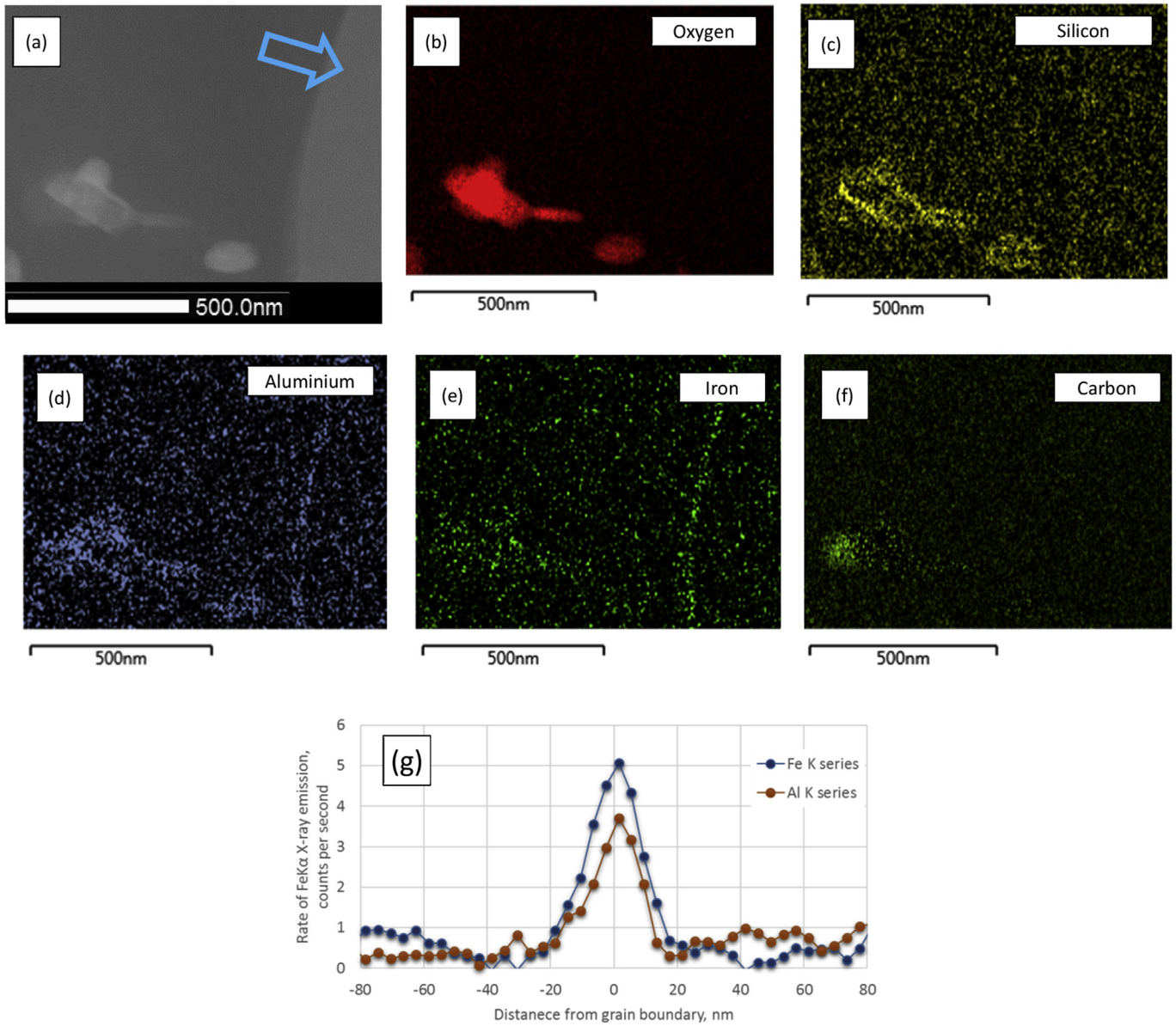

Fig. 6. (a) STEM image of the near-grain boundary area in PF-60 beryllium proton-irradiated to 0.45 dpa; (b–f) EDX elemental maps of the same area. Oxide particles, visible on the oxygen map (b) are enriched by other impurities and have Si and Al segregation on their surfaces.; (g) count rate profiles for Fe and Al taken across the grain boundary as shown by the blue arrow on (a).

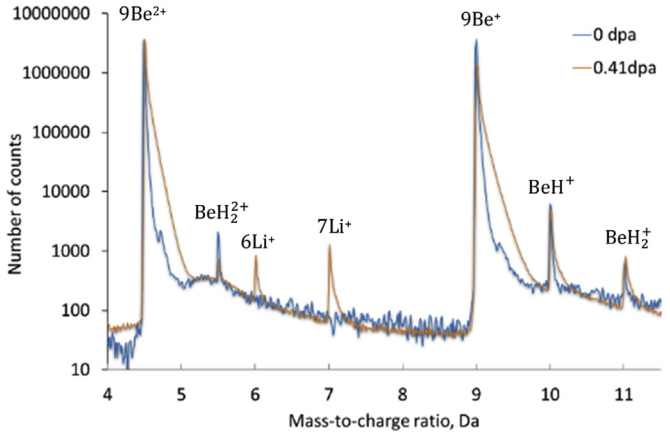

Fig. 7. Sections of the mass-spectra obtained from the PF-60 beryllium in as-received state (blue line) and after the irradiation in the NuMI beamline to 0.41 dpa (red line). The peaks at 6 and 7 Da can be assigned to lithium resulting from transmutation. (For interpretation of the references to colour in this figure legend, the reader is referred to the web version of this article.)

about 135 appm and 265 appm respectively. In samples made from areas irradiated to 0.46 dpa, these concentrations rise to 145 appm and 295 appm. These peaks cannot be assigned to any of expected beryllium contaminants, and result from transmutation during irradiation.

Since several isotopes of different elements can have the same mass:charge ratio and can overlap in mass-spectra, the usual APT procedures for isotopic separation are based on the values of their natural isotopic abundance [35,36]. However, this approach cannot be used for this case where the isotopes are created by transmutation. Calculations using the Monte Carlo based MARS code [30–32] were performed in order to quantitatively predict the concentrations of new isotopes created during proton irradiation and hence to assign chemical identities to the new peaks on the mass spectra. The measured matrix chemical composition for unirradiated material was used as the initial chemical state. Since new isotopes, when created, can themselves undergo radioactive decay, this was taken into account using the half-life data from Ref. [39].

Fig. 8 (a) shows the results of these calculations. Helium and hydrogen are the main transmutation products, with predicted production rates of about 4000 appm/dpa (He) and 3800 appm/dpa (H) and reaching about 2000 appm (He) and 1600 appm (H) in the central part of the NuMI beam window. Unfortunately, experimental validation of these predictions cannot be performed with APT. Helium is always lost during atom probe analysis. Hydrogen peaks can be identified but this element is very challenging for quantification in APT. It is a usual contaminant of the atom probe analysis chamber and its ions appear as peaks at 1 and 2 Da, which correspond to H^+ and H_2^+. Also hydrogen from the chamber may bond to adatoms at the specimen surface and then field-evaporate as beryllium hydride complexes BeH and BeH_2, which are observed in even the non-irradiated beryllium at 5.5, 10 and 11 Da (see Fig. 7). The probability of these events depends on the local electrical field at the surface of the APT needle and varies significantly within a single experiment and from one experiment to other. A number of studies have been dedicated to issues of detection and quantification of hydrogen with APT (see for example [40–42]), however, this problem is still not solved. Our studies showed an increase in H-related peaks in beryllium after irradiation, which may indicate that transmutant hydrogen isotopes also contribute to these peaks. Use of these data in combination with other techniques sensitive to hydrogen isotopes, such as SIMS [43] or Ion Beam Analysis [44], is needed for validation.

The third main transmutant predicted by MARS is lithium, with a production rate of about 850 appm/dpa. Two stable lithium isotopes, 6Li and 7Li, are created with predicted relative isotopic abundance of about 40%: 60%. No other isotopic candidates for peaks at 6 and 7 Da may be found from beryllium impurities or transmutants predicted by MARS, so the mass-spectrum peaks at 6 Da and 7 Da can be assigned to $6Li^+$ and $7Li^+$ ions. On the basis of this, during the proton irradiation in the neutrino source, about 400 appm (at 0.41dpa) and 440 appm (at 0.46dpa) of Li have been created in the beryllium (see Table 1). Fig. 8 shows that these experimental results on lithium are in good agreement with the quantities calculated by MARS. The measured relative abundance of 6Li and 7Li isotopes is about 35%: 65% which is close to the predicted values.

Lithium isotopes were homogeneously distributed in the beryllium matrix, as demonstrated by the 3D map of lithium distribution in Fig. 9a. The spatial randomness of Li atoms was verified and confirmed by a Nearest Neighbor (NN) analysis [36], as illustrated in Fig. 9b, where the observed distance distribution is in close match with its random comparator. χ^2 analysis, which estimates the deviation of an experimentally measured distribution from the binomial one [37], also confirmed that lithium is

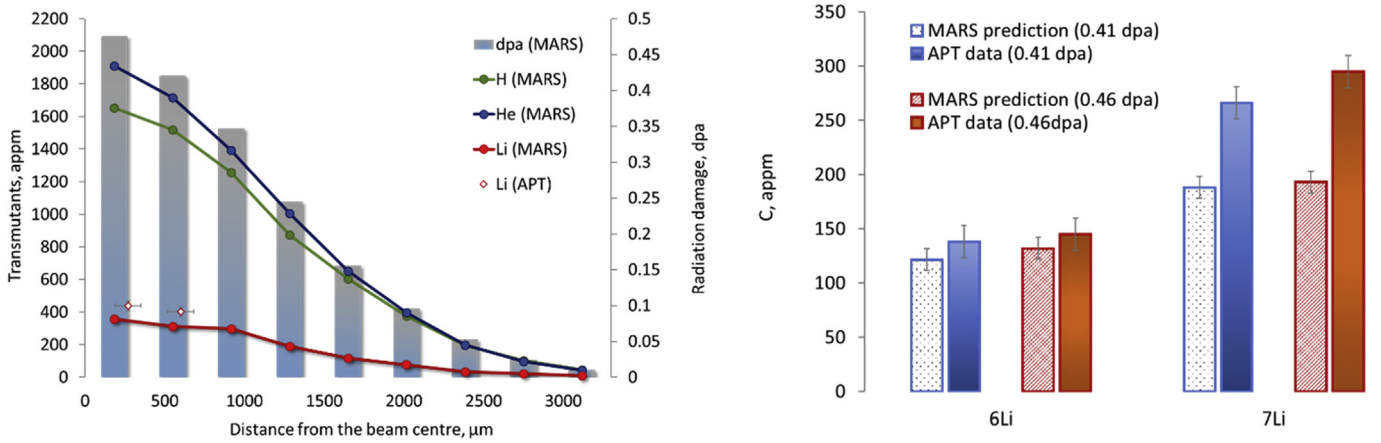

Fig. 8. (a) MARS simulation results for displacement damage and transmutation in the beryllium NuMI beam window after 7 years of operation as a function of distance from the centre of the proton beam. Two experimental points for lithium production are also shown, and are close to the predicted values; (b) comparison of the simulation results for production of lithium isotopes in different areas of the NuMI window with the experimental results obtained by APT.

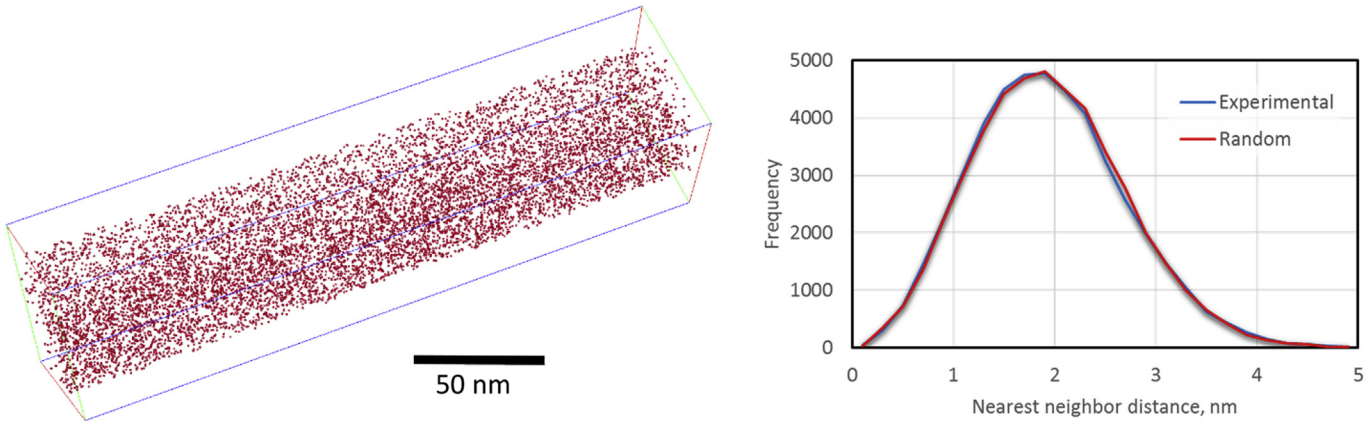

Fig. 9. (a) 3D map of lithium atoms distribution in the PF-60 beryllium irradiated in the NuMI beam line up to 0.41dpa. Any clustering of the transmutant is not noticeable; (b) Frequency histograms of the experimental and the randomly labelled first NN distance distributions of lithium atoms (the sampling width was 0.2 nm). The close match between observed and random distributions confirms that lithium atoms are randomly distributed in beryllium matrix.

homogeneously distributed in the beryllium matrix: the analysis of data from the experiment illustrated in Fig. 9 gave a p-value of 0.6 (the sampling box size was 100 atoms, with 114999 blocks analysed). Values less than $p = 0.05$ are commonly used standard values to reject the null hypothesis (i.e. "the solute is distributed randomly throughout the dataset") [37], thus, a random lithium distribution should be accepted.

While natural lithium may be present in PF-60 beryllium grade in quantities up to 4 appm [29], this value is significantly smaller than the observed amount. Moreover, natural lithium has a 6Li:7Li abundance close to 8%: 92% [45] that is very different from our experimental observations.

MARS also predicts creation by transmutation of various isotopes of B, C, O, Ne, Na, Mg, K, Ca, Mg, Fe, generally in sub-appm concentrations, but sometimes up to few appm in the very centre of the exposed window. APT experiments revealed a number of small peaks (typically less than 10 appm) on mass-spectra only in proton-irradiated parts of the beryllium window (see data in Table 1), which may belong to these minor transmutants. However, because of the small quantities of the detected ions, uncertainties in measurements and simulation, and potential influence of hydrogen-related and other artefacts of APT, it is not possible to assign the peaks unambiguously to specific transmutants.

3.3. *Fracture behaviour*

As described in section 2.1, the NuMI beam window was deformed in its central region during the procedure of punching-out from the flange, causing the development of radial cracks. The normal fracture mechanism of beryllium is by transgranular cleavage [5], but known to become predominately intergranular under exposure to neutron [46] or ion [17] irradiations. Crack paths were investigated by means of SEM/EBSD analysis in 6 different locations with the total crack path length of almost 600 μm. The data are summarised on Fig. 10(a). At least 85% of the length of the cracks in areas irradiated up to about 0.3 dpa is transgranular, as, for example, demonstrated on Fig. 10(b) where the area with a damage level of 0.29 dpa is shown. However, in zones with higher radiation doses, the fraction of crack length which follows grain boundaries increases; it is about 30% in regions exposed to 0.4 dpa and more than 50% in the most exposed areas with doses up to 0.48 dpa (see Fig. 10c). These limited statistics do not allow determination of an exact radiation exposure threshold of shift from intra-to inter-granular fracture, but shows a trend similar to the one observed in beryllium after neutron irradiation [46]. Further detailed investigations are ongoing.

4. Discussion

It is known that the chemistry, quantity and location of impurity precipitates in beryllium depends strongly on the purity and metallurgical history of a given sample [5]. The work presented here shows that impurities in as-manufactured beryllium PF-60 are highly inhomogeneously distributed.

Oxygen, the main impurity in beryllium, was also the main element in the most numerous family of clusters found, which other studies have found to be BeO particles [5]. It is known that solubility of oxygen in beryllium is very small, however precise values are unavailable. It is "believed to be" between 20 and 200 appm in Ref. [47] or "less than" 50 appm in Ref. [48]. Aldinger and Petzow (see section 7 in Ref. [5]) discus the physicochemical basis of the low solubility of O in Be and using an empirical relation propose a value of order of 10 appm. The atom probe data presented here show that a limited amount of oxygen (~70–90 appm) remains in solid solution in the beryllium matrix. Given that some fraction of this detected oxygen may come from possible oxygen contamination of the APT analysis chamber, our measurements are in good agreement with the available literature data.

Up to 450 appm of carbon may be in the PF-60 beryllium. Our STEM/EDX analysis show that carbon may enrich beryllium oxide particles and other types of clusters, but no carbon clusters were observed which could be identified as beryllium carbides. This may be related to the limitations of the EDX technique in identification of light elements and/or that any such clusters are only present at low number densities. The solubility of carbon in beryllium is not well established; values from 10 appm [5] to 35 appm [48] can be found in the literature. APT mass-spectra clearly indicated carbon peaks during analysis corresponding to about 15 appm, in reasonable agreement with the literature values. MARS predicted creation of an additional 5 appm of different carbon isotopes due to transmutation, but it was not possible to quantify carbon in the irradiated regions because of peak overlap with beryllium hydrides.

Iron impurity atoms were found in several different phases. Iron, found in precipitates with aluminium, was often enriched in beryllium oxide particles and segregated to grain-boundaries. Iron segregation to a dislocation line was also detected. Fe-containing precipitates have been previously experimentally observed at dislocations in beryllium [49], but to our knowledge, the APT data

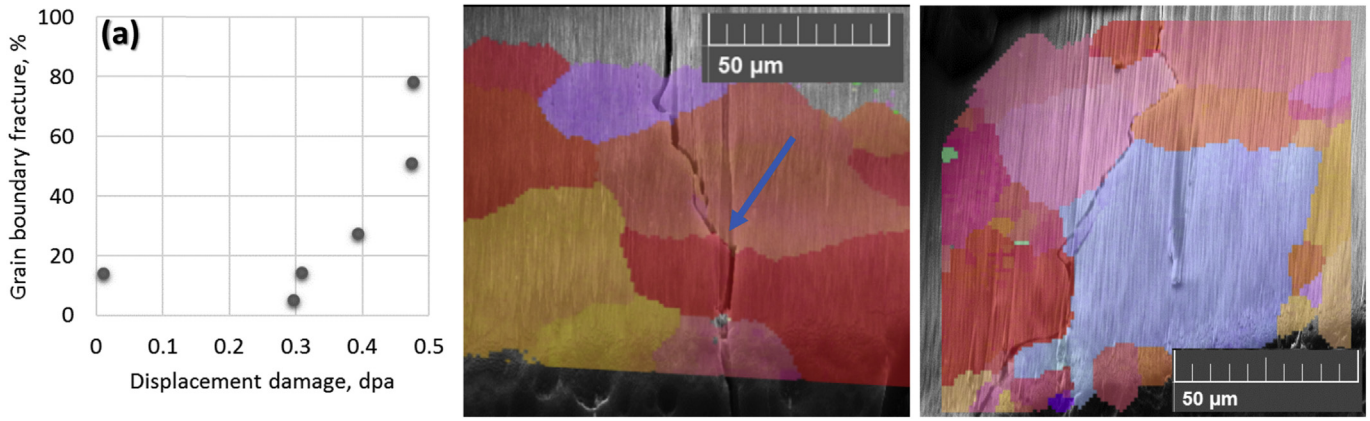

Fig. 10. (a) Measured fraction of grain boundary fracture and examples of crack paths through the NuMI beam window: (b) a region irradiated to 0.29 dpa and (c) a region irradiated to 0.47 dpa. Inverse pole EBSD maps are superposed on SEM images and demonstrate that at 0.29 dpa, only a small segment of the crack follows a grain boundary (highlighted by the blue arrow), whereas at 0.47 dpa, at least 75% of the crack follows grain boundaries. (For interpretation of the references to colour in this figure legend, the reader is referred to the web version of this article.)

presented here provide the first experimental evidence of Fe atmospheres at dislocations. Both Fe segregations and Fe-bearing precipitates at dislocation lines may be responsible for the yield point phenomenon in beryllium (see review [49] and references cited). A negative slope in the stress-strain curve after yielding is regularly observed in beryllium, but the consequences of this phenomenon are still debatable [5,49].

The solubility of iron is an important parameter for beryllium metallurgy since it determines the occurrence of phases responsible for dislocation pinning, hot shortness and fracture behaviour [5,9,50]. It is known to be substantially altered by presence of other alloying elements (especially aluminium) [5] and to depend strongly on temperature [51]. The solubility of iron in beryllium at 500 °C is reported to be 170 appm [51], but there are no experimental data in the literature for low temperatures. In the current study, 50 appm of iron was measured in solid solution in beryllium.

No silicon and aluminium impurities were detected by APT in solid solution; this is in good agreement with their known extremely low solubility in beryllium [5,52,53]. Both elements were detected in beryllium oxides, both in the cores of these precipitates and forming distinct Al-Si-rich shells on surfaces of large oxide particles. These Al-Si shells were too thin to allow the accurate measurement of their composition. The possibility of a low melting point Be-Al-Si eutectic in highly alloyed beryllium has been suggested [54], which might affect the stability of BeO particles [6], or, if present at grain boundaries, influence fracture behaviour [5,54]. However, this ternary phase has never been reported in commercial grades with low Al and Si contents.

Aluminium also forms precipitates, and many Al-Fe-enriched particles were detected in this beryllium grade. The detected Al:Fe atomic ratio ranged from 1:1.2 to 1:1.45, which may suggest that the observed phase may differ from the $AlFeBe_4$ or $FeAl_2Be_{2.3}$ phases reported in the literature [5,55,56]. However, very often the detected Al-Fe particles were located near Al-enriched oxide particles, and because of the averaging through the volume, EDX measurements may therefore overestimate the Al content. Aluminium is considered as one of the most harmful impurities in beryllium, since, in the form of free Al or Al-Be eutectic, it may wet grain boundaries and cause serious degradation of ductility at elevated temperatures (400 °C and above) [5]. All the Al-rich phases or Al segregation to grain-boundaries found in this study were also enriched by Fe, which is known to prevent low-melting point phase formation and thus maintain high-temperature ductility [5].

Because of the very high inhomogeneity of the PF-60 beryllium, the wide variety of impurity combinations and the limited sensitivity of EDS to low-Z elements, quantitative determination of the observed phase before and after irradiation was very difficult. Qualitatively, there appeared to be very few obvious changes in composition or distribution of existing impurities or precipitates as a result of irradiation.

The most pronounced proton-irradiation effect detected by APT was creation of transmutation products. Up to 440 appm of transmutant lithium were detected in the central part of the NuMI window, homogeneously distributed in the beryllium matrix, making this element a major non-gaseous impurity in solid solution in this beryllium grade post-irradiation. The effects of lithium on the properties of beryllium are currently not well understood, and have been the subject of little research. The only experimental data appear to be in the work of Kupriyanov [57] on beryllium samples annealed in contact with liquid lithium. It was demonstrated that penetration of lithium into beryllium can cause reduction of ultimate compressive strength and ductility. However, this is most likely due to lithium grain boundary diffusion and segregation rather than to any effects due to the solid solution of lithium in beryllium.

The atomic radius of beryllium is 112 pm and that of lithium is 167 pm (both are calculated values from Ref. [58,59]). This potentially makes lithium an effective element for solid solution strengthening if present in sufficient concentrations, however the concentrations measured here are low, and the effect might not be very significant. Aldinger [5] demonstrates that the experimental critical resolved shear stresses (CRSS) for basal slip in beryllium (its main deformation mechanism) and prismatic slip (secondary slip system) are proportional to $c^{2/3}$, where c is an impurity concentration in wt%, for wide range of impurity types. The full equations were not given, but analysis of the graphs in Ref. [5] gives, for Li in solution in Be: $CRSS_{BASAL} = 21.5 \times c^{\frac{2}{3}} + 1.38$ MPa and $CRSS_{PRISMATIC} = 28.5 \times c^{\frac{2}{3}} + 51$ MPa. Using these correlations, 400 appm of Li in the solid solution would be expected to lead to an increase of CRSS of approximately 2.1 MPa and 2.8 MPa for these two slip systems respectively. Petch and Wright [60] studied the relation between CRSS and macroscopic yield stress of vacuum-cast and extruded polycrystalline beryllium over the temperature range of 20–400 °C and showed that the ratio between σ_o (the 'intrinsic' yield stress, which enters to the Hall-Patch equation as a stress intercept) and the average value of CRSS for the basal and prismatic slip systems is about 4.3 (the so-called Taylor orientation factor

[61]). Hence the measured accumulation of lithium may result in a yield strength increase of approximately 11 MPa in polycrystalline beryllium.

No Li-Be compounds are known. No experimental results of solubility of lithium in beryllium are also known. Ref. [62] gives an assessed Li-Be phase diagram with an extremely small solubility of lithium in solid beryllium (miscibility line is undistinguishable from the Li = 0% ordinate) and stays very low even in the liquid state (less than 1% at 1300 °C). Considering the generally low solubility of impurity elements in beryllium and the significant difference in atomic sizes of Li and Be, at the concentrations measured here, up to 440 appm, lithium is most likely to be in a supersaturated solid solution; thus there should be a driving force towards precipitation. The temperature during radiation exposure was about 50 °C (= 0.27 T_m), and the diffusion kinetics at this temperature are likely to be insufficient for large-scale phase separation. However, even at the atom-probe scale (Fig. 9), there is no apparent tendency for the lithium to cluster. It is possible that individual Li atoms form stable complexes with vacancies or other defects produced by irradiation.

The next generation of proton accelerator particle sources, for example LBNF [63], significantly higher working temperatures for beryllium elements are projected, in the range 200–400 °C [1,3,4]. At these temperatures, vacancy-mediated diffusion in beryllium, possibly assisted by mobile radiation-induced defects, may lead to lithium precipitation in the Be matrix, and possibly at grain-boundaries. Even at room temperature, shear modulus of lithium is 4.2 GPa, only 3% of the shear modulus of beryllium. This makes potential lithium precipitates very soft objects inside the hard matrix or at grain boundaries. The melting point of bulk lithium is 181 °C; thus in the working temperature range of the LBNF, a grain boundary liquid phase, or one or very low shear strength, may be present that, similarly to conventional low melting point phases in beryllium (e.g. Al-Be/Al-Be-Si eutectics, or $MgBe_{13}$ [5]), may cause ductility losses or influence creep strength, but at lower temperatures. These considerations are also important for fusion irradiation environments, since a non-negligible quantity of Li can be produced in beryllium elements of fusion reactors [64].

The observed shift of the fracture mechanism from transgranular cleavage to grain-boundary cracking is a known radiation damage effect in beryllium and has been observed under neutron [46] and ion [17] irradiations. It is generally considered that the determining mechanisms here are helium segregation to grain boundaries at high temperature irradiations and the strengthening of the beryllium matrix by point defect clusters and/or nanometric gas bubbles at low temperatures [14–17]. Another grain-boundary softening mechanism was proposed in Ref. [18], based on anisotropy of stresses driven by non-homogeneous swelling of the hcp lattice. As shown in this paper, lithium ions in solid solution may also contribute to matrix strengthening, but this is a small effect and it is unlikely that any influence on fracture mechanisms will be significant at least at these levels of transmutation.

5. Conclusions and future work

Investigation of a beryllium high-energy accelerator window showed that unirradiated PF-60 beryllium is a highly textured and non-homogeneous alloy. Impurities are mainly localised in beryllium oxides and as precipitates inside beryllium grains. Limited amounts of oxygen, carbon, nickel, copper and iron are found in the solid solution. Iron also enriches grain-boundaries and dislocation lines. No noticeable changes in the distribution of these impurities were found after irradiation by high-energy protons up to 0.48 dpa at 50 °C. After irradiation, up to 440 appm of transmutant lithium was detected by APT, homogeneously distributed in the beryllium as a solid solution, making it one of the dominant impurities in this beryllium grade.

Investigation of post-irradiation crack paths indicates that proton irradiation at 0.4–0.5 dpa level changes the fracture mode from transgranular cleavage to grain-boundary cracking.

Future use of beryllium as target and beam window material in next generation particle accelerator facilities may be limited by higher dose and higher temperatures of operation. This work indicates that grain matrix hardening occurs at relatively modest DPA while lithium transmutant products remain homogenously distributed at the operating temperature of 50 °C. At higher dose and higher temperature, the nature of these phenomena may change, resulting in different limits of operation for Be components. For example, irradiation hardening may be countered by operating at higher temperatures in the 400–600 °C range where significant ductility is recovered. On the other hand, higher operating temperatures may lead to deleterious liquid phase lithium precipitates and/or He bubble formation at grain boundaries. Future work incorporating micro-mechanical techniques (nano-indentation or micro-cantilevers) at elevated temperature on this same material would help quantify the irradiation hardening effect in beryllium. In addition, examinations of beryllium material exposed to high energy proton irradiation at higher temperatures will shed light on the expected behaviour of Li and He transmutants. Such irradiated beryllium material may be available from the NOvA target, MET-02 (being put into operation now at Fermilab) and/or beryllium specimens planned to be irradiated at Brookhaven National Laboratory as part of the 2017 RaDIATE irradiation campaign.

Acknowledgments

This work supported by Fermi Research Alliance, LLC under Contract No. DE-AC02-07CH11359 with the United States Department of Energy and by the UK Science and Technology Facilities Council.

We thank our Fermilab colleagues Nikolai Mokhov, who provided expertise on MARS code that greatly assisted the research, Jim Hylen for neutrino yield operations performance estimates; and Frankie Kelly, Jim Wilson and Tony Busch for their help in recovering and extracting the irradiated NuMI Be window material.

We also thank Steven Van Boxel form the MRF (Culham, UK) for assistance with EBSD data treatment and Tomas Martin, Daniel Haley, Michael Moody from the University of Oxford (UK) for assistance with the APT experiments and data interpretation.

References

[1] P. Hurh, K. Ammigan, B. Hartsell, R. Tschirhart, Targetry Challenges at Megawatt Proton Accelerator Facilities, THPFI083, Proceedings of the 4th International Particle Accelerator Conference, (2013).
[2] RaDIATE Collaboration, (web-site). http://radiate.fnal.gov/..
[3] T. Davenne, O. Caretta, C. Densham, M. Fitton, P. Loveridge, P. Hurh, et al., Segmented beryllium target for a 2 MW super beam facility, Phys. Rev. Spec. Top. - Accel. Beams 18 (2015) 091003, http://dx.doi.org/10.1103/PhysRevSTAB.18.091003.
[4] Long-baseline Neutrino Experiment (LBNE) Project Conceptual Design Report Volume vol. 2: The Beamline at the Near Site, http://lbne.fnal.gov/, 2012.
[5] Beryllium Science and Technology, Springer Verlag, 2012.
[6] D. Webster, The effect of low melting point phases on the elevated temperature microstructural stability of hot pressed beryllium, Metall. Trans. A 6 (1975) 803–808, http://dx.doi.org/10.1007/BF02672303.
[7] A.W. Jones, R.T. Weiner, The effect of heat-treatment on the mechanical properties of some commercial beryllium, J. Common Met. 6 (1964) 266–282, http://dx.doi.org/10.1016/0022-5088(64)90123-7.
[8] J.S. Punni, M.J. Cox, The effect of impurity inclusions on the pitting corrosion behaviour of beryllium, Corros. Sci. 52 (2010) 2535–2546, http://dx.doi.org/10.1016/j.corsci.2010.03.024.
[9] S. Morozumi, N. Tsuno, S. Koda, Precipitation in beryllium-iron alloys, Trans. Jpn. Inst. Met. 10 (1969) 64–69.
[10] G.S. Was, Fundamentals of Radiation Materials Science: Metals and Alloys,

first ed., Springer, 2007.
[11] D.S. Gelles, H.L. Heinisch, Neutron damage in beryllium, J. Nucl. Mater 191–194 (Part A) (1992) 194–198, http://dx.doi.org/10.1016/S0022-3115(09)80032-9.
[12] V. Chakin, J. Reimann, A. Moeslang, R. Latypov, A. Obukhov, Thermal conductivity of highly neutron-irradiated beryllium in nuclear fusion reactors, Prog. Nucl. Energy 57 (2012) 2–7, http://dx.doi.org/10.1016/j.pnucene.2011.11.011.
[13] V.P. Chakin, A.O. Posevin, R.N. Latypov, Radiation damage in beryllium at 70–440°C and neutron fluence (0.3–18)·1022 cm−2 (E n > 0.1 MeV), At. Energy 101 (2006) 743–749, http://dx.doi.org/10.1007/s10512-006-0162-9.
[14] I.B. Kupriyanov, V.A. Gorokhov, R.R. Melder, Z.E. Ostrovsky, A.A. Gervash, Investigation of ITER candidate beryllium grades irradiated at high temperature, J. Nucl. Mater 258–263 (Part 1) (1998) 808–813, http://dx.doi.org/10.1016/S0022-3115(98)00383-3.
[15] S.A. Fabritsiev, A.S. Pokrovsky, R.M. Bagautdinov, Neutron irradiation effect on the mechanical properties and structure of beryllium, ResearchGate (1999) 1062–1076.
[16] A.S. Pokrovsky, S.A. Fabritsiev, R.M. Bagautdinov, Y.D. Goncharenko, High-temperature beryllium embrittlement, J. Nucl. Mater 233–237 (Part 2) (1996) 841–846, http://dx.doi.org/10.1016/S0022-3115(96)00027-X.
[17] W. Kesternich, H. Ullmaier, Mechanical properties and microstructure of helium-implanted beryllium, J. Nucl. Mater 312 (2003) 212–223, http://dx.doi.org/10.1016/S0022-3115(02)01637-9.
[18] G.A. Sernyaev, Radiation Damagebility of Beryllium, Ekaterinburg, 2001, 396 pages.
[19] M.R. Gilbert, S.L. Dudarev, S. Zheng, L.W. Packer, J.-C. Sublet, An integrated model for materials in a fusion power plant: transmutation, gas production, and helium embrittlement under neutron irradiation, Nucl. Fusion 52 (2012) 083019, http://dx.doi.org/10.1088/0029-5515/52/8/083019.
[20] S. Ohnuki, H. Takahashi, K. Shiba, A. Hishinuma, J.E. Pawel, F.A. Garner, Influence of transmutation on microstructure, density change, and embrittlement of vanadium and vanadium alloys irradiated in HFIR, J. Nucl. Mater 218 (1995) 217–223, http://dx.doi.org/10.1016/0022-3115(94)00382-3.
[21] S. Ohnuki, H. Takahashi, F.A. Garner, J.E. Pawel, K. Shiba, A. Hishinuma, Transmutation-induced embrittlement of vanadium and several vanadium alloys in HFIR, J. Nucl. Mater 233–237 (Part 1) (1996) 411–415, http://dx.doi.org/10.1016/S0022-3115(96)00335-2.
[22] F.A. Garner, L.R. Greenwood, B.A. Loomis, S. Ohnuki, N. Sekimura, Influence of flux-spectra differences on transmutation, dimensional changes and fracture of vanadium alloys, J. Nucl. Mater 233–237 (Part 1) (1996) 406–410, http://dx.doi.org/10.1016/S0022-3115(96)00227-9.
[23] F.A. Garner, L.R. Greenwood, D.J. Edwards, The influence of starting state on neutron induced density changes observed in Nb-1Zr and Mo-41Re at high exposures, J. Nucl. Mater 212–215 (Part 1) (1994) 426–430, http://dx.doi.org/10.1016/0022-3115(94)90098-1.
[24] D.J. Edwards, F.A. Garner, D.S. Gelles, The influence of neutron irradiation in FFTF on the microstructural and microchemical development of Mo–41Re at 470–730 °C, J. Nucl. Mater 375 (2008) 370–381, http://dx.doi.org/10.1016/j.jnucmat.2008.01.014.
[25] F.A. Garner, L.R. Greenwood, Neutron irradiation effects in fusion or spallation structural materials: some recent insights related to neutron spectra, Radiat. Eff. Defects Solids 144 (1998) 251–286, http://dx.doi.org/10.1080/10420159808229678.
[26] V. Kuksenko, C. Pareige, P. Pareige, Y. Dai, Production and segregation of transmutation elements Ca, Ti, Sc in the F82H steel under mixed spectrum irradiation of high energy protons and spallation neutrons, J. Nucl. Mater 447 (2014) 189–196, http://dx.doi.org/10.1016/j.jnucmat.2014.01.013.
[27] B. Long, Y. Dai, N. Baluc, Investigation of liquid LBE embrittlement effects on irradiated ferritic/martensitic steels by slow-strain-rate tensile tests, J. Nucl. Mater 431 (2012) 85–90, http://dx.doi.org/10.1016/j.jnucmat.2011.11.036.
[28] P. Adamson, K. Anderson, M. Andrews, R. Andrews, I. Anghel, D. Augustine, et al., The NuMI neutrino beam, Nucl. Instrum. Methods Phys. Res. Sect. Accel. Spectrom. Detect. Assoc. Equip. 806 (2016) 279–306, http://dx.doi.org/10.1016/j.nima.2015.08.063.
[29] PF-60 Beryllium Foil for X-ray, (web-site). http://materion.com/Products/Beryllium/BerylliumX-Ray/X-ray-PF-60.aspx.
[30] N.V. Mokhov, C. James, The MARS Code System User's Guide, 2016. https://mars.fnal.gov/.
[31] N.V. Mokhov, S.I. Striganov, MARS15 Overview, in: AIP, 2007, pp. 50–60, http://dx.doi.org/10.1063/1.2720456.
[32] Mokhov Nikolai, Aarnio Pertti, Eidelman Yury, Gudima Konstantin, Konobeev Alexander, Pronskikh Vitaly, et al., MARS15 code developments driven by the intensity frontier needs, Prog. Nucl. Sci. Technol. 4 (2014) 496–501.
[33] M.J. Norgett, M.T. Robinson, I.M. Torrens, A proposed method of calculating displacement dose rates, Nucl. Eng. Des. 33 (1975) 50–54, http://dx.doi.org/10.1016/0029-5493(75)90035-7.
[34] N.V. Mokhov, Beam–materials interactions, Rev. Accel. Sci. Technol. 06 (2013) 275–290, http://dx.doi.org/10.1142/S1793626813300132.
[35] M.K. Miller, Atom Probe Tomography: Analysis at the Atomic Level, Kluwer Academic/Plenum Publishers, New York, 2000.
[36] B. Gault, M.P. Moody, J.M. Cairney, S.P. Ringer, Atom Probe Microscopy, Springer Series in Materials Science, 2012.
[37] M.P. Moody, L.T. Stephenson, A.V. Ceguerra, S.P. Ringer, Quantitative binomial distribution analyses of nanoscale like-solute atom clustering and segregation in atom probe tomography data, Microsc. Res. Tech. 71 (2008) 542–550, http://dx.doi.org/10.1002/jemt.20582.
[38] H.P. Rooksby, I.R. Green, The identification and determination of foreign phases and constituents in metals, with special reference to beryllium, Analyst 87 (1962) 539–547, http://dx.doi.org/10.1039/AN9628700539.
[39] G. Audi, O. Bersillon, J. Blachot, A.H. Wapstra, The Nubase evaluation of nuclear and decay properties, Nucl. Phys. A 729 (2003) 3–128, http://dx.doi.org/10.1016/j.nuclphysa.2003.11.001.
[40] J. Takahashi, K. Kawakami, Y. Kobayashi, T. Tarui, The first direct observation of hydrogen trapping sites in TiC precipitation-hardening steel through atom probe tomography, Scr. Mater 63 (2010) 261–264, http://dx.doi.org/10.1016/j.scriptamat.2010.03.012.
[41] D. Haley, S.V. Merzlikin, P. Choi, D. Raabe, Atom probe tomography observation of hydrogen in high-Mn steel and silver charged via an electrolytic route, Int. J. Hydrog. Energy 39 (2014) 12221–12229, http://dx.doi.org/10.1016/j.ijhydene.2014.05.169.
[42] H. Takamizawa, K. Hoshi, Y. Shimizu, F. Yano, K. Inoue, S. Nagata, et al., Three-Dimensional characterization of deuterium implanted in silicon using atom probe tomography, Appl. Phys. Express 6 (2013) 066602, http://dx.doi.org/10.7567/APEX.6.066602.
[43] Y. Oya, Y. Hirohata, Y. Morimoto, H. Yoshida, H. Kodama, K. Kizu, et al., Hydrogen isotope behavior in in-vessel components used for DD plasma operation of JT-60U by SIMS and XPS technique, J. Nucl. Mater 313–316 (2003) 209–213, http://dx.doi.org/10.1016/S0022-3115(02)01451-4.
[44] N. Kubota, K. Ochiai, C. Kutsukake, K. Kondo, W.M. Shu, M. Nishi, et al., Ion and neutron beam analyses of hydrogen isotopes, Fusion Eng. Des. 81 (2006) 227–231, http://dx.doi.org/10.1016/j.fusengdes.2005.09.022.
[45] T.B. Coplen, J.K. Böhlke, P. De Bièvre, T. Ding, N.E. Holden, J.A. Hopple, et al., Isotope-abundance variations of selected elements (IUPAC Technical Report), Pure Appl. Chem. 74 (2002), http://dx.doi.org/10.1351/pac200274101987.
[46] L.L. Snead, Low-temperature low-dose neutron irradiation effects on beryllium, J. Nucl. Mater 326 (2004) 114–124, http://dx.doi.org/10.1016/j.jnucmat.2003.12.016.
[47] J.P. Pemsler, R.W. Anderson, E.J. Rapperport, Textron Inc West Concord MA Nuclear Metals Div, Solubility and Diffusion of Gases in Beryllium, Defense Technical Information Center, Ft. Belvoir, 1963.
[48] K.A. Walsh, Beryllium Chemistry and Processing, ASM International, 2009.
[49] D.R. Floyd, Causes of the yield-point phenomenon in commercial beryllium products. http://www.osti.gov/servlets/purl/4309095/, 1974 (Accessed 9 May 2016).
[50] E. Levine, G. Lütjering, Precipitation in the beryllium-iron system, J. Common Met. 23 (1971) 343–357, http://dx.doi.org/10.1016/0022-5088(71)90044-0.
[51] S.M. Myers, J.E. Smugeresky, Phase equilibria and diffusion in the Be-Al-Fe, Metall. Trans. A 7 (1976) 795–802, http://dx.doi.org/10.1007/BF02644075.
[52] H. Okamoto, Be-Si (Beryllium-Silicon), J. Phase Equilibria Diffus. 30 (2009) 115, http://dx.doi.org/10.1007/s11669-008-9433-6, 115.
[53] H. Okamoto, Al-Be (Aluminum-Beryllium), J. Phase Equilibria Diffus. 27 (2006) 424–425, http://dx.doi.org/10.1007/s11669-006-0025-z.
[54] M. Weisz, J. Mallen, J.L. Baron, Possibilite d'apparition d'une phase liquide a partir de 430° C dans le beryllium commercial, J. Nucl. Mater 10 (1963) 56–59, http://dx.doi.org/10.1016/0022-3115(63)90116-8.
[55] P.J. Black, The structure of *T* (AlFeBe), Acta Crystallogr. 8 (1955) 39–42, http://dx.doi.org/10.1107/S0365110X55000108.
[56] H.P. Rooksby, Intermetallic phases in commercial beryllium, J. Nucl. Mater 7 (1962) 205–211, http://dx.doi.org/10.1016/0022-3115(62)90166-6.
[57] I.B. Kupriyanov, V.N. Kudryavtsev, L.A. Kurbatova, I.E. Lyublinski, Effect of high temperature corrosion in liquid lithium on mechanical properties of beryllium, Fusion Eng. Des. 85 (2010) 1702–1706, http://dx.doi.org/10.1016/j.fusengdes.2010.05.006.
[58] E. Clementi, D.L. Raimondi, Atomic screening constants from SCF functions, J. Chem. Phys. 38 (1963) 2686, http://dx.doi.org/10.1063/1.1733573.
[59] E. Clementi, Atomic screening constants from SCF functions. II. Atoms with 37 to 86 electrons, J. Chem. Phys. 47 (1967) 1300, http://dx.doi.org/10.1063/1.1712084.
[60] N.J. Petch, E. Wright, The plasticity and cleavage of polycrystalline beryllium. I. Yield and flow stresses, Proc. R. Soc. Math. Phys. Eng. Sci. 370 (1980) 17–27, http://dx.doi.org/10.1098/rspa.1980.0019.
[61] S.G.I. Taylor, Plastic Strain in Metals, 1938.
[62] A.D. Pelton, The Be–Li (Beryllium-Lithium) system, Bull. Alloy Phase Diagr. 6 (1985) 30–32, http://dx.doi.org/10.1007/BF02871175.
[63] J. Strait, E. McCluskey, T. Lundin, J. Willhite, T. Hamernik, V. Papadimitriou, et al., Long-baseline Neutrino Facility (LBNF) and Deep Underground Neutrino Experiment (DUNE) Conceptual Design Report, vol. 3, 2016. Long-Baseline Neutrino Facility for DUNE June 24, 2015, ArXiv160105823 Hep-Ex Physics-sphysics, http://arxiv.org/abs/1601.05823 (Accessed 5 December 2016).
[64] C.B.A. Forty, R.A. Forrest, G.J. Butterworth, Activation of beryllium in a fusion power plant, J. Nucl. Mat. 258–263 (Part 1) (1998) 793–797, http://dx.doi.org/10.1016/S0022-3115(98)00117-2.